

Kink-Antikink Interaction Forces and Bound States in a nonlinear Schrödinger Model with Quadratic and Quartic dispersion

G. A. Tsolias,¹ Robert J. Decker,² A. Demirkaya,² T.J. Alexander,³ Ross Parker,⁴ and P. G. Kevrekidis¹

¹*Department of Mathematics and Statistics, University of Massachusetts, Amherst, MA 01003-4515, USA*

²*Mathematics Department, University of Hartford,
200 Bloomfield Ave., West Hartford, CT 06117, USA*

³*Institute of Photonics and Optical Science (IPOS),
School of Physics, The University of Sydney, NSW 2006, Australia*

⁴*Department of Mathematics, Southern Methodist University, Dallas, TX 75275, USA*

In the present work we explore the competition of quadratic and quartic dispersion in producing kink-like solitary waves in a model of the nonlinear Schrödinger type bearing cubic nonlinearity. We present the first 6 families of multikink solutions and explore their bifurcations as the strength of the quadratic dispersion is varied. We reveal a rich bifurcation structure for the system, connecting two-kink states with states involving 4-, as well as 6-kinks. The stability of all of these states is explored. For each family, we discuss a “lower branch” adhering to the energy landscape of the 2-kink states. We also, however, study in detail the “upper branches” bearing higher numbers of kinks. In addition to computing the stationary states and analyzing their stability within the partial differential equation model, we develop an effective particle ordinary differential equation theory that is shown to be surprisingly efficient in capturing the kink equilibria and normal (as well as unstable) modes. Finally, the results of the bifurcation analysis are corroborated by means of direct numerical simulations involving the excitation of the states in a targeted way in order to explore their instability-induced dynamics.

I. INTRODUCTION

In the study of nonlinear dispersive waves, arguably one of the most well-established models with a wide range of possible applications is the nonlinear Schrödinger equation [1–3]. Its relevance extends from mean-field limits of atomic gases [4–6], to the propagation of the envelope of the electric field in optical fibers [7, 8] and from water waves [3] to plasmas [9] and beyond. Nevertheless, recent studies have recognized the experimental relevance and theoretical interest in exploring realms beyond those of purely quadratic dispersion, as accompanying the prototypical cubic nonlinearity (stemming from the Kerr effect [8] or the s-wave scattering of bosons [4, 5]).

More concretely, over the past few years, a new direction within nonlinear optics has stemmed from the ability to engineer dispersion in optical systems in the laboratory, potentially completely eliminating quadratic dispersion and enabling quartic dispersion to be dominant [10]. This has led to the experimental observation of the so-called pure-quartic solitons (PQS) [10] and subsequently the realization of the pure-quartic soliton laser [11]. Numerous other possibilities have emerged from this research thread, including, but not limited to, the ability to program dispersion of higher order in fiber lasers [12], the possibility to explore the competing interaction of quadratic and quartic dispersion for bright [13–15] or dark/kink-like solitary waves [16, 17], and the study the self-similar propagation of pulses in the presence of gain [18] or their nature in the absence of Galilean invariance [19]. It should be noted that some of these topics (especially with regards to bright solitary waves) have been the focus of earlier well-known works [20, 21]. It is also noteworthy that a number of studies have explored the existence and stability of solutions in related models bearing 4th order dispersion (or competing dispersions), as well as their potential for collapse [22–24].

In the present work we revisit this interesting class of models, aiming to offer a systematic exploration of the branches of kink-like (dark-soliton [25]) excitations in the presence of quadratic and quartic competing dispersions. A short description of the relevant features was presented in [16]. Here, we systematically expand upon the branches of solutions noted in this earlier work and examine the bifurcation of these solutions in detail. Indeed, we examine the first 6 families of states among the ones possible, classified on the basis of the separation between the kink and the antikink. Our emphasis is not on the simpler single branch of kink solutions, but rather on the considerably more elaborate feature of the quadratic-quartic model, namely the possibility of existence of multi-kink bound states. We start from the simpler 2-kink states, which form the so-called “lower branches” of our bifurcation diagrams and continue the solutions in one of the key parameters of the system, namely the strength of the quadratic dispersion. For all of the relevant families (except for the “exceptional” 0th family which seems to emanate from the small amplitude limit), the branches feature a characteristic turning point which leads to an “upper branch” of states. The latter nucleates either one or two pairs of additional kinks, leading to states involving 4-kink and 6-kink solutions. We identify all of these states systematically and present a comprehensive overview of their stability properties. Equally importantly, in the limit of large β_2 (the quadratic dispersion parameter), we develop a theoretical formulation of the interacting kinks as “effective particles” (see, e.g., also our earlier considerations in [17]). This, in turn, allows us to identify the equilibrium configurations and their kink locations in the resulting interacting particle system, and examine the linear properties of these particles around the equilibria. We find that this particle picture is remarkably accurate at capturing the unstable and stable modes of the multi-kink states. Whenever relevant, we also complement the existence and stability studies with dynamical computations exploring the fate of the unstable states.

Our presentation will be structured as follows. In Section II, we will provide the general theoretical framework of the problem and the methodology for exploring the multi-kink interacting particle system. In Section III, the center-theme of our work, we provide the existence and stability analysis, and compare our theoretical results with those obtained from dynamical simulations. Finally, in Section IV, we summarize our findings and offer some directions for further study. In the Appendix, some of the details of our numerical computations are systematically provided for the reader that is more keenly interested in the practical aspects of the numerical methods.

II. MODEL SETUP AND ANALYSIS

The generalized variant of the nonlinear Schrödinger (GNLS) equation that we study in the present work is [16]:

$$iu_t + \frac{\beta_4}{4!} u_{xxxx} - \frac{\beta_2}{2} u_{xx} + \gamma |u|^2 u = 0, \quad (1)$$

where in an optical context β_4 characterizes the strength of the fourth-order dispersion, β_2 the strength of the second-order dispersion and γ the strength of the cubic nonlinearity. We focus on the so-called quartic normal dispersion regime, where stable dark solitons have been found [16] in the presence of attractive nonlinearity, and so take $\beta_4 > 0$ and $\gamma > 0$. Later we will restrict to $\beta_4 = 1$ and $\gamma = 1$.

A. Stationary States and Spectral Stability

Eq. (1) is a Hamiltonian system, with conserved energy \mathcal{E} given by

$$\mathcal{E}(u) = \frac{1}{2} \int_{-\infty}^{\infty} \left(\frac{\beta_4}{4!} |u_{xx}|^2 + \frac{\beta_2}{2} |u_x|^2 + \frac{\gamma}{2} |u|^4 \right) dx. \quad (2)$$

Separating real and imaginary parts by taking $u = u_R + iu_I$, Eq. (1) can be written in standard Hamiltonian form as

$$\frac{\partial u}{\partial t} = J\mathcal{E}'(u(t)), \quad (3)$$

where $u = (u_R, u_I)^T$, $\mathcal{E}'(u(t))$ is the functional derivative of $\mathcal{E}(u)$ evaluated at $u(t)$ and J is the standard symplectic matrix

$$J = \begin{bmatrix} 0 & 1 \\ -1 & 0 \end{bmatrix}. \quad (4)$$

Eq. (3) then becomes the pair of real-valued equations

$$(u_R)_t = -\frac{\beta_4}{24}(u_I)_{xxxx} + \frac{\beta_2}{2}(u_I)_{xx} - (u_R^2 + u_I^2)u_I \quad (5)$$

$$(u_I)_t = \frac{\beta_4}{24}(u_R)_{xxxx} - \frac{\beta_2}{2}(u_R)_{xx} + (u_R^2 + u_I^2)u_R. \quad (6)$$

In what follows, we are interested in stationary (time-independent amplitude) solutions of the form: $u(x, t) = e^{i\mu t}\phi(x)$. Substituting this ansatz into (1), we get the steady state model for the amplitude ϕ

$$\frac{\beta_4}{4!}\phi'''' - \frac{\beta_2}{2}\phi'' - \mu\phi + \gamma\phi^3 = 0. \quad (7)$$

In addition to the solution $\phi = 0$, Eq. (7) has continuous wave (CW) solutions $\phi = \pm\sqrt{\mu/\gamma}$.

To facilitate our understanding of the nature of these fixed points, we rewrite (7) as a system of four first-order ordinary differential equations, using $U = (u_1, u_2, u_3, u_4) = (\phi, \phi', \phi'', \frac{\beta_4}{24}\phi''')$. Eq. (7) then becomes the first order system in \mathbb{R}^4

$$U' = F(U) = \begin{bmatrix} u_2 \\ u_3 \\ \frac{24}{\beta_4}u_4 \\ \frac{\beta_2}{2}u_3 + \mu u_1 - \gamma u_1^3 \end{bmatrix}. \quad (8)$$

For $\beta_4 > 0$, $\mu > 0$, and all β_2 , the linearization about $\phi = 0$ has a pair of real eigenvalues $\pm\alpha$ and a pair of imaginary eigenvalues $\pm\beta i$, thus the corresponding equilibrium of (8) has a two-dimensional center subspace, and $\phi = 0$ is a saddle-center fixed point. The eigenvalues of the linearization about the CW states $\phi = \pm\sqrt{\mu/\gamma}$ are instead

$$\lambda = \pm\sqrt{\frac{6\beta_2 \pm 2\sqrt{9\beta_2^2 - 12\beta_4\mu}}{\beta_4}}.$$

For fixed $\beta_4 > 0$ and $\mu > 0$, corresponding equilibria $S^\pm = (\pm\sqrt{\mu/\gamma}, 0, 0, 0)$ are saddle points of (8) when $\beta_2 > -\beta_2^*$, where

$$\beta_2^* = 2\sqrt{\frac{\beta_4\mu}{3}}. \quad (9)$$

The stable and unstable manifolds of S^\pm are both two-dimensional. When $|\beta_2| < \beta_2^*$, the spatial eigenvalues are a complex quartet $\pm a \pm bi$, topologically corresponding to a saddle-spiral, and when $|\beta_2| > \beta_2^*$, they are two pairs of real eigenvalues $\pm b_1$ and $\pm b_2$, leading to a saddle point in the four dimensional space.

In our computations that will follow, the conditions $-\beta_2^* < \beta_2 < \beta_2^*$ will play a pivotal role providing a set of bounds for β_2 under which the kink-antikink states of interest will exist. Later we will restrict our attention to the specific case of $\mu = 5$.

A kink ϕ_k is a solution to (7) connecting the CW state at $-\sqrt{\mu/\gamma}$ (S^-) to the one at $\sqrt{\mu/\gamma}$ (S^+). From a spatial dynamics perspective, this is a heteroclinic orbit connecting the saddle points S^- and S^+ . If ϕ is a solution to (7), so is $-\phi$, thus for every kink solution ϕ_k there is a corresponding anti-kink $-\phi_k$. When $\beta_4 = 0$ and $\beta_2 > 0$, the exact formula for the stationary kink is given by

$$\phi_k(x) = \sqrt{\frac{\mu}{\gamma}} \tanh\left(\sqrt{\frac{\mu}{\beta_2}} x\right). \quad (10)$$

We take the existence of a primary kink solution to (7) as a hypothesis in what follows.

To study the stability of these solutions, we consider the linearization around $u(x, t) = e^{i\mu t}\phi(x)$, where $\phi(x)$ is a solution to (7). Adding the perturbation as follows $u(x, t) = e^{i\mu t}[\phi(x) + v(x, t)]$, where $v(x, t) = v_R + iv_I$, substituting it into (1), we obtain two equations:

$$\begin{aligned} (v_R)_t &= -\frac{\beta_4}{4!}v_I'''' + \frac{\beta_2}{2}v_I'' + \mu v_I - \gamma\phi^2 v_I \\ (v_I)_t &= \frac{\beta_4}{4!}v_R'''' - \frac{\beta_2}{2}v_R'' - \mu v_R + 3\gamma\phi^2 v_R \end{aligned}$$

which can be written as

$$\frac{\partial}{\partial t} \begin{bmatrix} v_R \\ v_I \end{bmatrix} = \begin{bmatrix} 0 & -\mathcal{L}_-(\phi) \\ \mathcal{L}_+(\phi) & 0 \end{bmatrix} \begin{bmatrix} v_R \\ v_I \end{bmatrix} = -J\mathcal{L}(\phi) \begin{bmatrix} v_R \\ v_I \end{bmatrix}, \quad (11)$$

where

$$\begin{aligned} \mathcal{L}_+(\phi) &= \frac{\beta_4}{4!}D^4 - \frac{\beta_2}{2}D^2 - \mu + 3\gamma\phi^2 \\ \mathcal{L}_-(\phi) &= \frac{\beta_4}{4!}D^4 - \frac{\beta_2}{2}D^2 - \mu + \gamma\phi^2 \\ \mathcal{L}(\phi) &= \begin{bmatrix} \mathcal{L}_+(\phi) & 0 \\ 0 & \mathcal{L}_-(\phi) \end{bmatrix}. \end{aligned}$$

In what follows we find the lowest six families (as defined in Section III) of stationary kink-antikink solutions numerically and examine their stability using Eq. (11).

B. Effective Particle Model

Using a method due to N. Manton [26], we now derive an ODE model of kink - antikink interaction. For our model the Lagrangian is

$$L = \int_{-\infty}^{\infty} \mathcal{L} dx = \int_{-\infty}^{\infty} \left(\frac{i}{2}(u_t^* u - u^* u_t) - \frac{\beta_2}{2}u_x^* u_x - \frac{\beta_4}{4!}u_{xx}^* u_{xx} - \frac{1}{2}\gamma|u|^4 \right) dx. \quad (12)$$

Invariance under translations gives rise to the conserved quantity

$$P = \int_{-\infty}^{\infty} \frac{i}{2} (u_x^* u - u^* u_x) dx \quad (13)$$

which is the total momentum P of the field u . In order to calculate the force F between a kink and an antikink, we consider the momentum included in a finite interval $[x_1, x_2]$ and we differentiate with respect to time t .

$$\begin{aligned} F &= \frac{dP}{dt} = \int_{x_1}^{x_2} \frac{i}{2} (u_{xt}^* u + u_x^* u_t - u_t^* u_x - u^* u_{xt}) dx \\ &= \int_{x_1}^{x_2} i (u_x^* u_t - u_t^* u_x) dx + \frac{i}{2} [u_t^* u - u^* u_t]_{x_1}^{x_2} \\ &= \left[\frac{\beta_2}{2}u_x^* u_x - \frac{\beta_4}{4!}(u_x^* u_{xxx} - u_{xx}^* u_{xx} + u_{xxx}^* u_x) - \frac{\gamma}{2}|u|^4 + \frac{i}{2}(u_t^* u - u^* u_t) \right]_{x_1}^{x_2} \end{aligned} \quad (14)$$

For $u(t, x) = e^{i\mu t} \phi(x)$, where $\phi(x)$ is a real static field this expression simplifies to

$$F = \left[\frac{\beta_2}{2} \phi'^2 + \frac{\beta_4}{4!} (\phi''^2 - 2\phi' \phi''') - \frac{\gamma}{2} \phi^4 + \mu \phi^2 \right]_{x_1}^{x_2} = F_{x_2} - F_{x_1} \quad (15)$$

which is zero, as expected for a static solution (the quantity inside the brackets is constant if ϕ satisfies Eq. (7)).

Now, suppose we have a superposition of a kink centered at $x = -X$ and an antikink centered at $x = X$. Then the force on the antikink due to the kink is given by Eq. (15) for $x_1 = 0$ and $x_2 \rightarrow \infty$, i.e., integrating across the antikink to find the force exerted on it due to the change of its momentum.

For $x_2 \rightarrow \infty$, let $\phi \rightarrow -\sqrt{\mu/\gamma}$. Then,

$$F_{x_2} = \frac{\mu^2}{2\gamma} \quad (16)$$

For x in the region between the two kinks, let $\phi(x) = \sqrt{\mu/\gamma} - \eta(x)$, for η small. Then keeping up to second order terms we get

$$F_{x_1} \approx \left[\frac{\beta_2}{2} \eta'^2 + \frac{\beta_4}{4!} (\eta''^2 - 2\eta' \eta''') + \frac{\mu^2}{2\gamma} - 2\mu\eta^2 \right]_{x=0} \quad (17)$$

Therefore the force acting on the antikink is given in terms of $\eta(x)$ by the following expression:

$$F \approx \left[-\frac{\beta_2}{2} \eta'^2 - \frac{\beta_4}{4!} \eta''^2 + \frac{\beta_4}{4!} 2\eta' \eta''' + 2\mu\eta^2 \right]_{x=0} \quad (18)$$

If X is large enough, so that the two kinks are well separated, then $\eta(x)$ can be very well approximated by the superposition of their tails. In particular, for large positive x , a single kink can be written as $\phi_K(x) = \sqrt{\frac{\mu}{\gamma}} - \chi(x)$ (and similarly, for large negative x a single antikink can be written as $\phi_{AK}(x) = \sqrt{\frac{\mu}{\gamma}} - \chi(-x)$), where the tail $\chi(x)$ satisfies the linearized problem

$$2\mu\chi - \frac{\beta_2}{2} \chi'' + \frac{\beta_4}{4!} \chi'''' = 0 \quad (19)$$

For $\beta_2 < 2\sqrt{\frac{\beta_4\mu}{3}}$ the linearized equation has vanishing solutions of the form

$$\chi(x) = e^{-rx} (A \cos(kx) + B \sin(kx)) \quad (20)$$

where

$$r = \sqrt{\frac{2\sqrt{3\beta_4\mu} + 3\beta_2}{\beta_4}} \quad \text{and} \quad k = \sqrt{\frac{2\sqrt{3\beta_4\mu} - 3\beta_2}{\beta_4}}. \quad (21)$$

Then, the superposition of the tails gives

$$\sqrt{\frac{\mu}{\gamma}} - \eta(x) = \phi(x) \approx \phi_K(x + X) + \phi_{AK}(x - X) - \sqrt{\frac{\mu}{\gamma}}, \quad (22)$$

from which we obtain

$$\eta(x) \approx \chi(x + X) + \chi(-x + X) \quad (23)$$

Substituting this into Eq. (18) and using Eq. (20), we finally get

$$F \approx e^{-2rX} \left(\left(2(A^2 - B^2) \frac{r^2 k^2 \beta_4}{3} + 4ABrk\beta_2 \right) \cos(2kX) + \left(4AB \frac{r^2 k^2 \beta_4}{3} - 2(A^2 - B^2)rk\beta_2 \right) \sin(2kX) \right) \quad (24)$$

For an effective ODE description we need to find the inertial mass of the kinks. For c small enough, our numerical computations of traveling kinks suggest that the field u configuration can be written as $u(x, t) = e^{i\mu t} (\phi_K(x - ct) - c^2 v(x - ct) + ic w(x - ct))$. This corresponds to the profile of a kink ϕ_K moving to the right

with constant speed c , since $|u|^2 = \phi_K^2(x - ct) + \mathcal{O}(c^2)$, while w denotes to the leading order imaginary (linear in c) and v the leading order real (quadratic in c) correction.

Now, from Eq. (1) we get

$$i(u_t^* u + u^* u_t) = -\frac{\beta_2}{2}(u_{xx}^* u - u^* u_{xx}) + \frac{\beta_4}{4!}(u_{xxxx}^* u - u^* u_{xxxx}) \quad (25)$$

and since $|u|^2$ is a function of $x - ct$, the time derivative can be expressed as a spatial derivative multiplied by $-c$.

$$i(u_t^* u + u^* u_t) = i(|u|^2)_t = -ic(|u|^2)_x \quad (26)$$

Integrating over x gives

$$-ic|u|^2 = -\frac{\beta_2}{2}(u_x^* u - u^* u_x) + \frac{\beta_4}{4!}(u_{xxx}^* u - u_{xxx}^* u_x + u_x^* u_{xx} - u^* u_{xxx}) - icK \quad (27)$$

where K is an integrating real constant. Of course, for this equation to hold as $x \rightarrow \infty$, we need $K = \frac{\mu}{\gamma}$. Integrating one more time over the whole x -axis and rearranging the terms, we get:

$$\int_{-\infty}^{\infty} \frac{\beta_2}{2}(u_x^* u - u^* u_x) dx = -ic \int_{-\infty}^{\infty} \left(\frac{\mu}{\gamma} - |u|^2 \right) dx + \frac{\beta_4}{4!} \int_{-\infty}^{\infty} (u_{xxx}^* u - u_{xxx}^* u_x + u_x^* u_{xx} - u^* u_{xxx}) dx \quad (28)$$

Then the total momentum of the traveling kink is given by

$$P = \frac{c}{\beta_2} \int_{-\infty}^{\infty} \left(\frac{\mu}{\gamma} - |u|^2 \right) dx + \frac{\beta_4 c}{12\beta_2} \int_{-\infty}^{\infty} (\phi_K w''' - \phi_K' w'' + \phi_K'' w' - \phi_K''' w) dx + \mathcal{O}(c^2) \quad (29)$$

and using the definition $P = Mc$ for the inertial mass we find

$$M = \frac{1}{\beta_2} \int_{-\infty}^{\infty} \left(\frac{\mu}{\gamma} - \phi_K^2 \right) dx + \frac{\beta_4}{12\beta_2} \int_{-\infty}^{\infty} (\phi_K w''' - \phi_K' w'' + \phi_K'' w' - \phi_K''' w) dx \quad (30)$$

where w must satisfy

$$-\mu w - \frac{\beta_2}{2} w'' + \frac{\beta_4}{4!} w'''' + \gamma \phi_K^2 w = \phi_K' \quad (31)$$

In what follows, we will consider the mass that solely stems from the first term of Eq. (30), i.e., the standard renormalized mass of the defocusing NLS problem (that has also been used, e.g., towards the proof of the stability of the dark solitons thereof in, e.g., [27]). This will be justified a posteriori via the comparison of our results with the detailed numerical computations. A rigorous justification of this choice from first principles is an interesting topic for future study.

III. NUMERICAL RESULTS AND COMPARISON

We now restrict our attention to numerical solutions of Eq. (7) with $\mu = 5$, $\gamma = 1$, and $\beta_4 = 1$. Letting β_2 vary, we get families of solutions to Eq. (7), where the members of each family are connected by numerical continuation with respect to β_2 . We start by finding kink-antikink solutions at $\beta_2 = 0$ corresponding to larger and larger separation of the kink and antikink, as in [16]. We then use numerical continuation to create families of solutions which we refer to as family 0 (continuation of the smallest possible separation of kink-antikink at $\beta_2 = 0$), family 1 (continuation of the second smallest possible separation of kink-antikink at $\beta_2 = 0$), and so on for families 2, 3, 4, and 5. Additional families have been identified in our numerical computations, however to keep the presentation more succinct, we do not discuss them here.

An overarching summary of our results is shown in Fig. 1. Here we see that each family of solutions has both an upper and lower branch, which are connected by numerical continuation, with the exception of family 0, where the upper branch was not created as a numerical continuation of the lower branch. Before we delve into the details of individual branches, we identify the main features encompassing all the branches on the figure. Throughout our analysis we make use of the complementary power Q to characterize the families of solutions,

$$Q = \int_{-L}^L \left(\frac{\mu}{\gamma} - \phi^2 \right) dx, \quad (32)$$

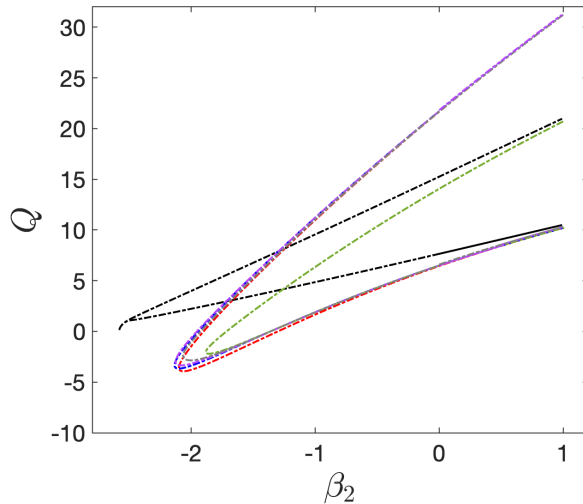


FIG. 1. Bifurcation diagrams of six families of solutions: family 0 (black), family 1 (red), family 2 (blue), family 3 (green), family 4 (purple), family 5 (gray). In all cases $\mu = 5$, $\gamma = 1$, and $\beta_4 = 1$.

where L is the half-width of the stationary solution domain. This is effectively the same quantity as the one defined by M in the previous section, however to more clearly distinguish between the two (bearing in mind that in the latter there is, in principle, also a contribution $\propto \beta_4$, we use a different symbolism here.

We can see on the right side of Fig. 1, as $\beta_2 \rightarrow 1$, that the branches form 3 groups, with each group distinguished by the number of kinks present (2, 4 and 6 in increasing complementary power). The lowermost group involves what we will hereafter term “lower branches” for all the families considered below. This concerns the states involving 2 kinks that are well-separated in this large and positive β_2 limit. The next group, encompassing solely family 0 (black upper branch) and family 3 (green upper branch), involves solutions consisting of 4 kinks. Finally, after a similar “jump” in complementary power, we encounter all remaining upper branches (e.g., the red of family 1, the blue of family 2, the purple of family 4 and the gray of family 5), which are all solutions with 6 kinks. These results relate to the large and positive β_2 limit, but in the case where β_2 becomes negative, we encounter a similar partition between the branches. Namely, the black and green branches are somewhat “special”. The former tends to a limit of progressively smaller complementary power, i.e., tending to a small-amplitude steady oscillation about the CW solution itself, while the latter has a turning point β_2^{cr} which is distinct from that of all other branches. However the 4 remaining branches (1, 2, 4 and 5) seem quite similar at the level of this complementary power diagnostic. For these 4 branches all solutions starting on a lower branch feature a turning point for a negative value of β_2 (near -2) and subsequently continue along an upper branch towards the 6-kink configuration discussed above. A final observation that we make based on earlier analysis [16] is that the CW is modulationally stable whenever $\beta_2 \geq 0$, but when $\beta_2 < 0$ there is a continuous band of modulationally unstable wavenumbers with bounds $k = \pm \sqrt{-12\beta_2/\beta_4}$. Indeed, the relevant branch(es) can never be stable for $\beta_2 < 0$. We now turn to details of each of the relevant families.

A. Family 0

We start by describing the family 0 presented in the bifurcation diagram of Fig. 2 and the dynamics plots of Fig. 3. Fig. 2(a) illustrates the profiles and spectral planes of the stability analysis associated with this branch for different values of β_2 . If we look at the zoomed in bifurcation diagram on the right, Fig. 2(b), we see that the states appear to bifurcate from the CW background as localized wavepackets (with increasing β_2), for both the lower and upper branches. These branches tend to a small oscillation about the fixed point $\sqrt{\mu/\gamma}$ (for decreasing β_2), of approximately 0.04, as β_2 tends to $\beta_2^* \approx -2.58$. This limiting amplitude gets smaller as the simulated x -domain gets larger (for double the size of the x -domain this amplitude is approximately 0.02) and so it is reasonable to assume that the limiting steady state flattens out as the size of the x -domain approaches infinity.

Following the lower branch to increasing β_2 (lower panels of Fig. 2(a)) we see that the state can be described as a kink-anti-kink pair with an increasing separation distance. Indeed, the analysis of [17] which is generalized in Sec. II B, shows that the quartic dispersion induces an oscillatory tail in the kinks which (competing with the quadratic

dispersion), in turn, enables the possibility of bound states between two kink-like structures. This landscape consists of an alternation of local energy minima (such as the present one), forming center points in the landscape of the soliton center dynamics, and local energy maxima, which, naturally, correspond to saddle points in the relevant landscape. For the centers like the one corresponding to the lower bifurcation branch, we expect stability, at least as far as the motion of the kink centers is concerned, and indeed we see in the bottom right of Fig. 2(a) that there are no instability eigenvalues (when $\beta_2 > 0$).

Turning our attention now to the upper branch in Fig. 2 we see that this corresponds to a state consisting of four kinks (i.e., four zeros in the amplitude at large β_2), but it also bifurcates from the nearly flat state at $\beta_2^* \approx -2.58$. Indeed, it appears (see the bottom insets of Fig. 2(b)) that the two and 4 kink states merge, in the sense of the complementary power Q , in the small amplitude limit (about the CW). In contrast to the lower branch however, the upper branch appears to always be unstable. Recall that for this family, the upper branch is not a numerical continuation of the lower branch (as is the case for the other families) but rather is calculated the same way that the lower branch is calculated, using a numerical continuation from a carefully chosen initial steady state at $\beta_2 = 0$.

While an oscillatory eigenvalue quartet seems to exist, we will not discuss such instabilities at length, as they appear in our computations to be strongly dependent on the computational domain size. Indeed, similarly to other such examples in the realm of dark solitons (starting with the work of [28]), the presence of so-called anomalous modes, pertaining to the motion of the solitary waves, inside the continuous spectrum gives rise to such resonances which are domain-size dependent as the latter determines the (finite-domain-induced) “quantization” of the continuous spectrum. On the other hand, we observe that the 4 kinks have 3 internal modes in their dynamics (in addition to their translational motion which is neutral and pertains to a so-called Nambu-Goldstone mode associated with the corresponding invariance). Indeed, for the 2 kinks, there is only one motion, in addition to their neutral translation, namely the out-of-phase relative motion thereof, while generally for N kinks, we should expect $N - 1$ such internal modes associated with the kink relative motions. In the case of the upper branch of family 0, Fig. 3 elucidates the situation. In particular, its right panel uses the approach pioneered by Manton [26] and analyzed above in Sec. II B to identify the equilibrium kink configuration and performs a linearization analysis around it, in the form of a 4×4 system to obtain the effective particle normal modes. Two of these are oscillatory (featuring one pair moving towards each other and one away from each other), while the third is an unstable real mode with the kinks moving in opposite outward directions. The kinks centered in the positive half-line move in unison and so do the ones in the negative half-line, but these two pairs move in opposite directions between them. This instability can lead to a splitting of the 4-kink bound state into two 2-kink bound states as shown in Fig. 3(a), but it can also lead all 4 to collide at the center, featuring a long-lived breathing state before eventually separating. Notice that, as explained in the inset, in each of these dynamical evolution cases, we will present the case example where we have added the unstable eigenvector to the configuration, and also the one where we have subtracted it. These two possibilities have been used in order to seed the instability in two opposite directions, as seen in panel (a) of the figure and, similarly, in other examples of such seeding presented below.

B. Families 1, 3, 5

These families are grouped together as they concern *unstable* saddle configurations in their respective lower branches, as is clearly manifested in each of the bottom right insets in panels (a)-(c) in Fig. 4. Indeed, in each case the two-kink configurations pertain to the first, the second and the third local maxima of the energy landscape associated with the two 2-kink states which means that their out-of-phase motion should give rise to a dynamical instability. Consequently the two bottom right insets in each branch feature the associated real pair with a corresponding eigenmode that should dynamically destabilize the relevant state. As we move towards negative β_2 , once again the modulational instability discussed previously takes place and all relevant configurations are unstable due to the continuous spectrum portion lying along the real axis.

Each of the relevant families features a turning point beyond which we move to the upper portion of the corresponding branches. These branches feature 6 kinks for the families 1 and 5 and 4 kinks for the family 3. As discussed previously, family 3, along with family 0 are special in this regard, while all other families feature 6 kink states in their upper portions.

To better understand this we need to turn our focus to the single kink bifurcation diagram. As we move to the left along the lower branch (and β_2 decreases), undulations on the oscillating tails on both sides of the kink increase in size. When the largest undulation (of which there are two, one on each side, due to symmetry) reaches a critical size, we reach the turning point. Then as we move on to the upper branch, (and now β_2 increases), the undulations decrease in size, except for the two largest ones. These continue to grow and eventually give rise to the two new kink pairs, one on each side of the kink.

Two-kink solutions behave in a similar manner, but the number and the location of the new kink pairs depend on

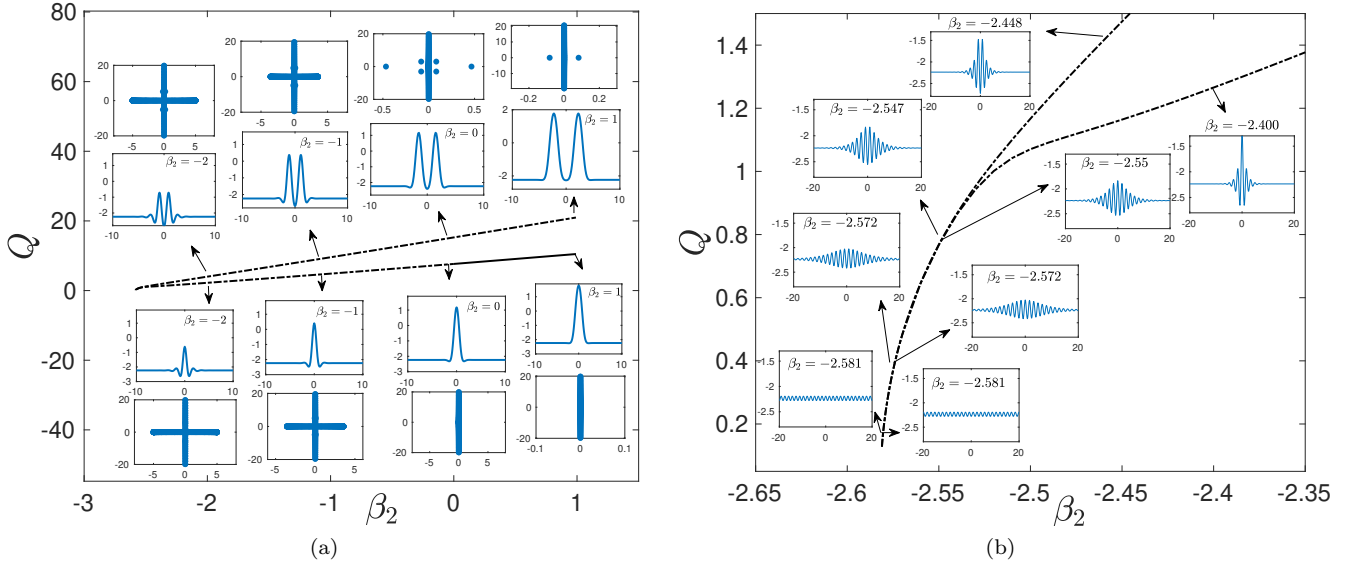


FIG. 2. (a) Bifurcation diagram (Q vs β_2), the corresponding steady state solutions and spectra for Family 0, presented for a sequence of values of the quadratic dispersion parameter β_2 . (b) the same bifurcation diagram as (a) but zoomed in about the intersection of the upper and the lower curves.

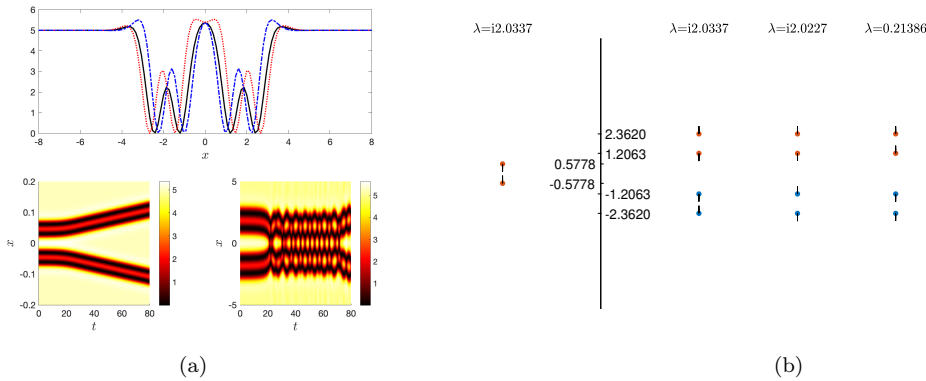


FIG. 3. PDE and ODE initial conditions and dynamics for family 0 (upper branch only for PDE). The upper figure of (a) shows the plots of $\|u\|^2$ (black), $\|u + v_1\|^2$ (red), and $\|u - v_1\|^2$ (blue) for $\beta_2 = 0.5$, where v_1 is the eigenfunction corresponding to the only real PDE eigenvalue of 0.2231. The lower left panel of (a) is the contour plot that results from using $\|u + 0.01v_1\|^2$ as the initial condition, and the lower right panel of (a) is the contour plot that results from using $\|u - 0.01v_1\|^2$ as the initial condition. (b) gives the ODE values for the soliton positions (left of vertical line is the lower branch, right of the vertical line is the upper branch) and the ODE eigenvalues along the top (again lower branch left and upper branch right). Arrows on the points indicate the initial directions of the solitons (all directions would be reversed if v_1 is replaced by $-v_1$.)

the distance between the two original kinks. That distance can only be such that the oscillating tails between the two kinks interfere either constructively (odd families) or destructively (even families). In the latter case, the two largest undulations will be the ones outside of the kink pair and these will give rise to the two new kink pairs. In the former case, the two largest undulations will be the ones inside the kink pair, *if* there is enough space to do so, as in families 5, 7, 9... , where two new pairs appear in the region inside the two kinks. In the case of family 3, there is space for only one new pair to appear, while in the case of family 1 there is no space for any such pair at all, so the new pairs can appear from the undulations outside the two original kinks.

The interference between the oscillating tails of the two kinks can also explain the differences between the value of β_2^{cr} of each family. In the constructive case, the largest undulations reach their critical size earlier, as we move to the

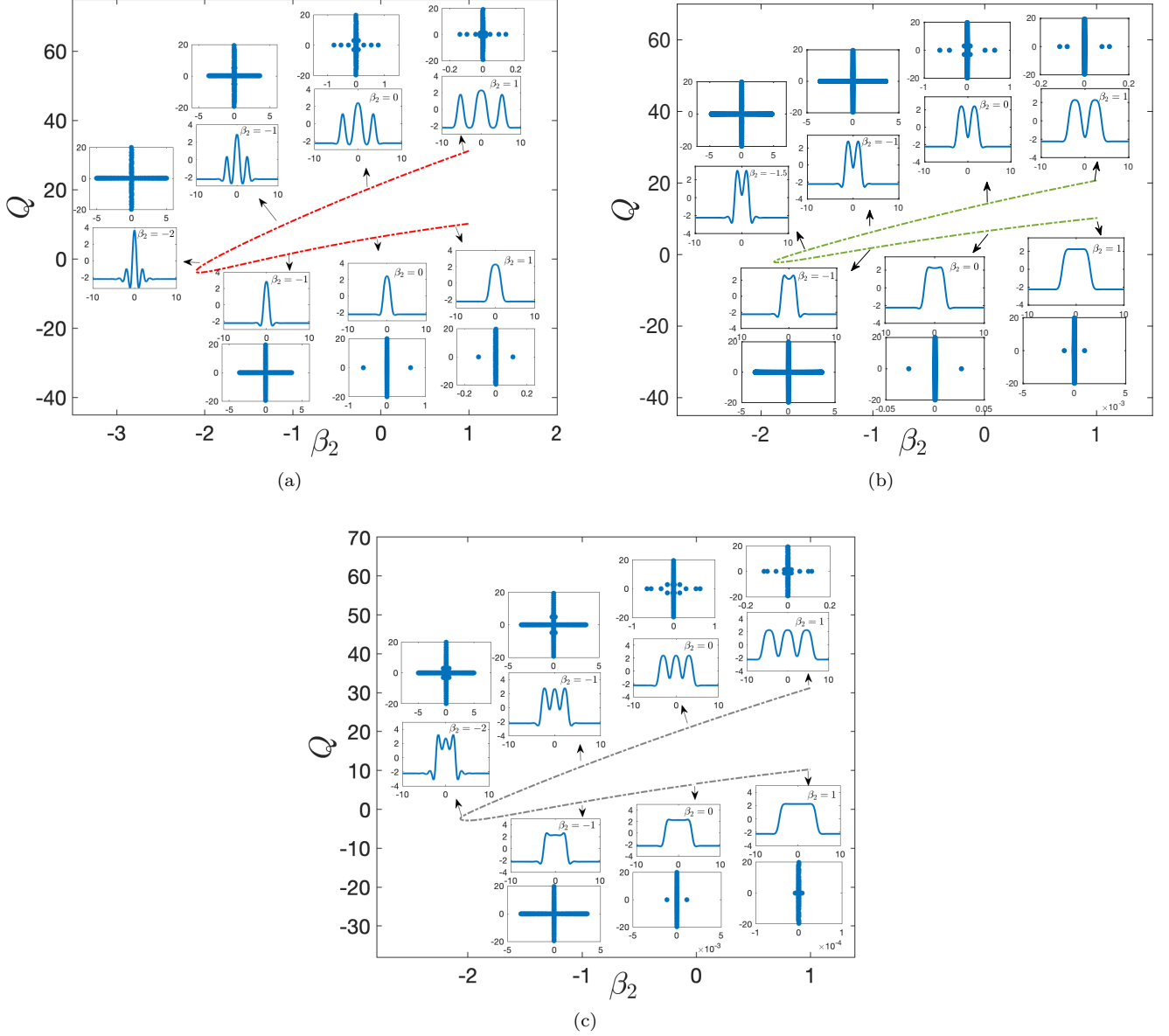


FIG. 4. Bifurcation diagram and the corresponding steady state solutions and spectrums for a) family 1, b) family 3, c) family 5.

left. So we reach the turning point for larger β_2 , compared to the single kink case. In the destructive case, on the other hand, undulations are smaller so we need to move further to the left for them to reach their critical size. So the turning point corresponds to β_2 smaller than the one in the single kink case (with the notable exception of family 1).

It should be added here that for the families 0 and 1, we have also depicted the phase portrait of the plane (u, u_x) of Fig. 5. The aim of the figure is to showcase how for family 0, the kink-antikink profile only loops around 0, but does not make it to loop around the (spatial) fixed point of $-\sqrt{\mu/\gamma}$, while in the case of family 1, that looping does (as the first such example among the families) take place. The effectively self-similar pattern of the spatial configuration as it loops around the saddle-spiral fixed point at $u = \sqrt{\mu/\gamma}$ is further illustrated in the zooms of panels (b) and (c).

Turning now to the upper branch of family 1, the analysis of the relevant state is conveyed in Fig. 6. Panel (d) summarizes our theoretical predictions. More concretely, the 6-kink state features 2 oscillatory modes and 3 real ones, in addition to the neutral translational one. The one with the largest growth rate (≈ 0.391) features an out-of-phase motion of the two innermost kinks, while the other 4 remain essentially immobile. This instability is showcased in

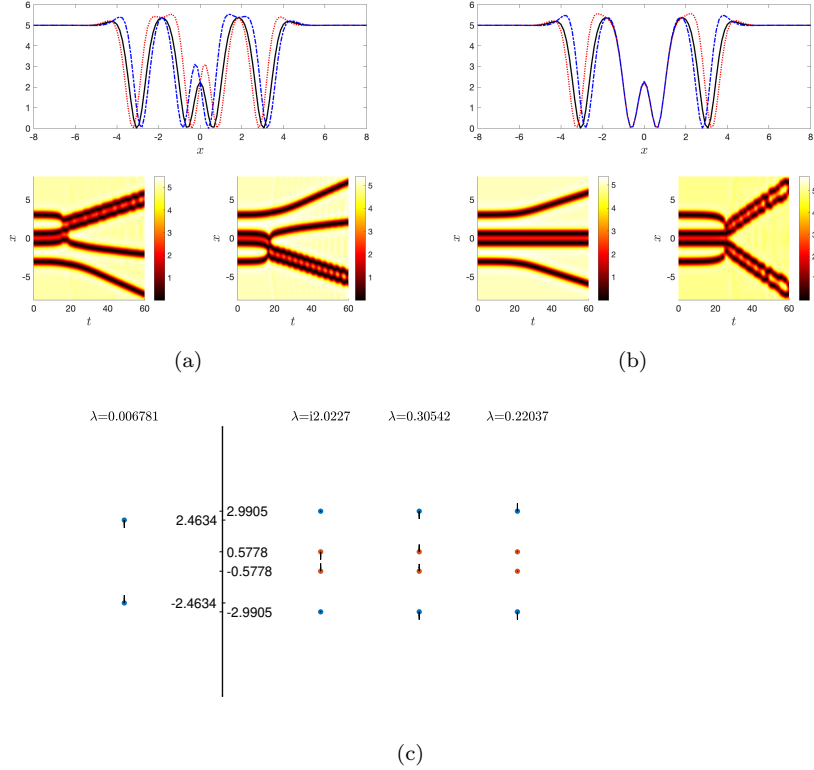


FIG. 7. PDE and ODE initial conditions and dynamics for Family 3 (upper branch only for PDE). Similar to Figure 6, except for Family 3 instead of Family 1, with $\beta_2 = 0.5$ and PDE eigenvalues (a) λ_1 : 0.3083 and (b) λ_2 : 0.2104.

the dynamical evolution of panel (a) where we see that these inner kinks may either move outward colliding with the other two pairs (and forming breathing pairwise bound states, while the outermost kink is expelled) or they may move inward, collide and then move outward again, leading to the same fate as the previous example. We have also excited the two other unstable modes in panel (b) (for growth rate ≈ 0.267) and panel (c) (with growth rate ≈ 0.12), respectively. In the former case, the two inner kinks move in one direction, while the four outer ones move in the opposite direction. In both shown examples of panel (b), this leads to collisions and pairwise formations of one kink with a bound state pair. In each example where this happens, there is a “change of allegiance”. The pair member closest to the single kink now forms a bound state with the formerly single kink, while the pair member furthest from the single kink is now “freed” and moves in the direction that the single kink used to move. In the case of the eigenmode excited in panel (c) the outer kinks move outward or inward, while the centermost pair stays put. However, what ends up being observed is more akin to the dynamics of panel (a), which appears to be the dominant instability, since the associated eigenmode growth rate is a factor of (nearly) 4 times larger than the eigenmode initially excited in panel (c). See also the discussion surrounding the case example shown later in Fig. 13(e).

In the case of family 3, the corresponding dynamical picture is provided in Fig. 7. The lower branch situation is again simple (with the out-of-phase motion of the two kinks predicted in panel (c) being responsible for the instability of this saddle-point configuration at a larger distance of ≈ 2.46 at equilibrium. However, as indicated above, this is an example whereby the upper branch involves only 4 kinks. In this setting, our effective particle theory predicts the existence of 2 unstable modes with growth rates ≈ 0.305 and ≈ 0.22 . The largest growth rate involves the inner kinks moving in one direction and the outer ones in the opposite, as shown in panel (a) of the figure. This leads, in line with what we saw before, to the collision of the inner pair with one of the outer kinks, and once again the same phenomenon of “change of allegiance” as discussed above. The less rapid growth is associated with a mode whereby the inner kinks stay put while the outer ones move either outward or inward (depending on the sign of the perturbation), as shown in panel (b). Among these cases, the outward motion is more “benign” as the outer kinks depart to (in principle) infinity, while the inner kinks remarkably are sitting at the equilibrium distance of the lower branch of family 0 and, hence, will stay at that distance indefinitely given the stability of the latter configuration. A far more elaborate scenario takes place when the outer kinks first move inward. In this case they collide with the

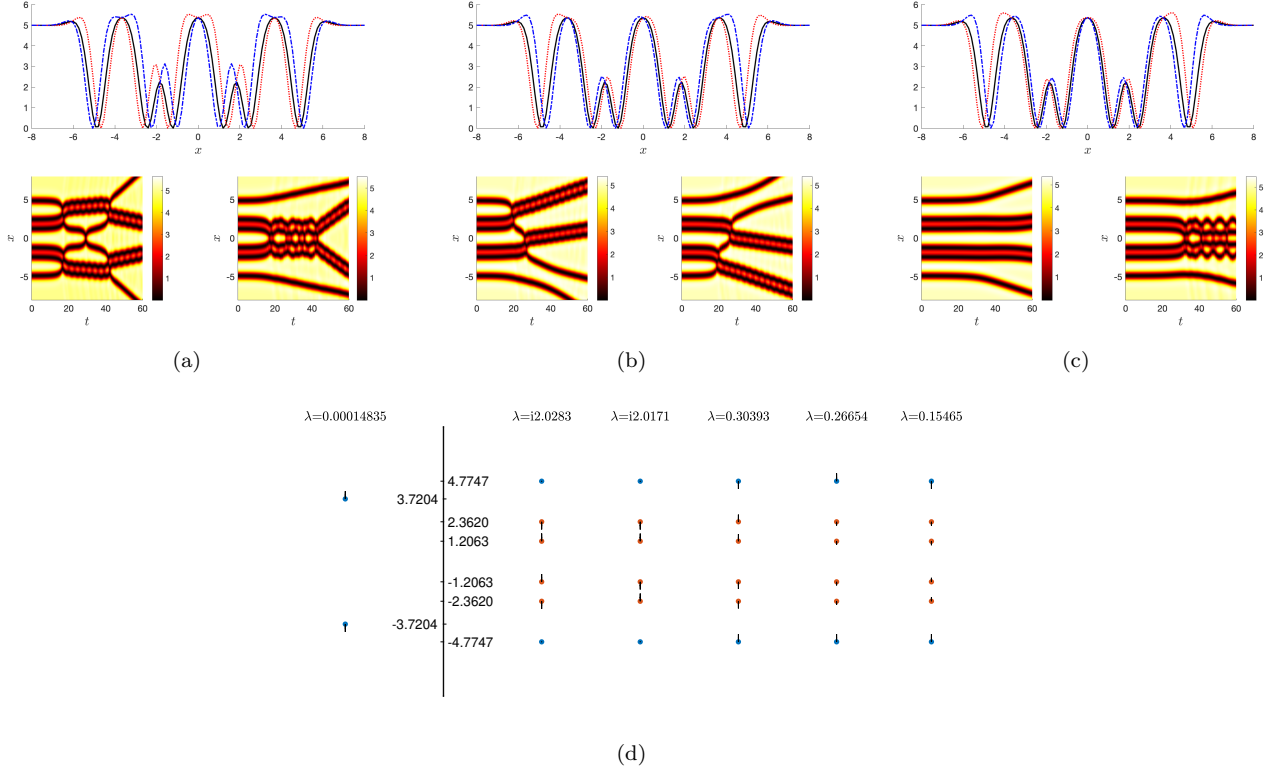


FIG. 8. PDE and ODE initial conditions and dynamics for Family 5 (upper branch only for PDE). Similar to Figure 6, except for Family 5 instead of Family 1, with $\beta_2 = 0.5$ and PDE eigenvalues (a) λ_1 : 0.3105, (b) λ_2 : 0.2640, and (c) λ_3 : 0.1509.

central kinks leading to an expulsive event where, pairwise, two sets of kinks (the upper and lower ones, so to speak) are expelled outward in a breathing, propagating state. While this seems like a nearly bound state, the distance between the kinks appears to be increasing as they move suggesting that it does not pertain to a stable configuration. Nevertheless, an exploration of such breathing, propagating states could be an interesting topic for future study, as it is outside the scope of the present work.

We now turn to family 5, which again like most families has 6 kinks in its upper portion (in addition to 2 substantially separated kinks at distance of ≈ 3.72 in its saddle-configuration lower portion). Here again, we encounter a situation involving 3 unstable modes of the upper branch, along with 2 oscillatory ones which have also been included for completeness in Fig. 8, in addition to the neutral translational mode. The unstable modes have growth rates of ≈ 0.304 , 0.267 and 0.155 as indicated in panel (d) of the figure. The most unstable among these modes involves the out-of-phase motion of the two inner kink pairs of this configuration and the opposite to them, also out-of-phase motion of the outer kink pair. This can lead, as shown in panel (a) of the figure, e.g., to a collision of the kink pairs with the outer kinks, leading to a change of allegiance and then complex dynamics since the split innermost kinks collide between them and then again with the breathing pairs (leading to further change of allegiance etc.). In the case of the two pairs moving inward they collide with each other, while the outer kinks move outward. In this case, the complex dynamics of the 4-kink collision near the center eventually leads, upon breathing, to two outer moving and breathing pairs, once again reminiscent of the ones we saw in family 3. Again, such dynamics as well as similar pair breathing and propagating, for instance, in panel (b) of the figure are motivating towards further study of such states. The case of panel (b) involves a weak in-phase motion of the 4 inner kinks and a stronger opposite direction motion of the 2 outer ones. This leads to a collision of one of the outer kinks with one of the inner pairs, and then a resulting cascade of two changes of allegiance as observed in both instances of panel (b) resulting eventually in two breathing pairs moving in one direction and two isolated kinks in the opposite direction. Finally, the weakest unstable mode of panel (c) involves all kinks for $x > 0$ moving in the same direction and similarly all those for $x < 0$ moving in the opposite direction. In the first example of panel (c) this leads to no collisions with the kinks continuing to move in their original direction. In the second example, all kinks move towards the center and the two pairs collide there, leading to a breathing long-lived excitation, while the outer kinks initially moving inward are eventually led,

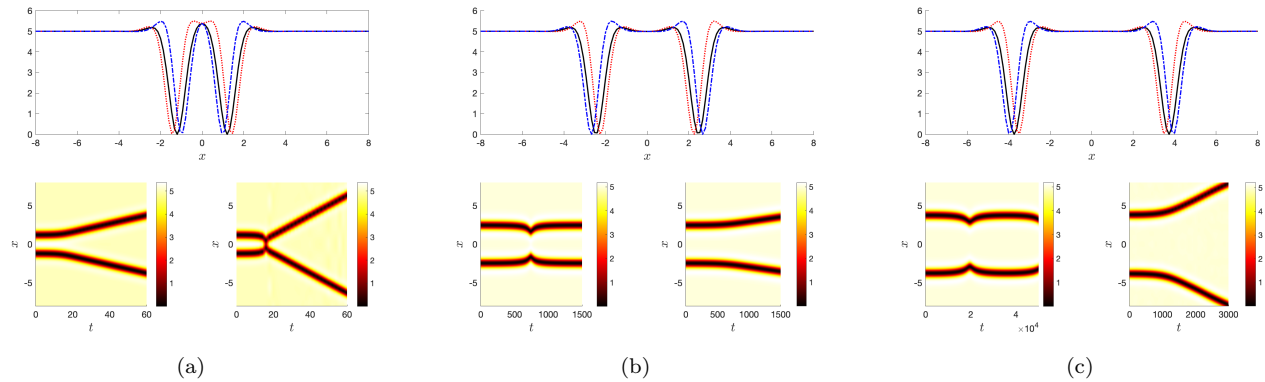


FIG. 9. PDE initial conditions and dynamics for lower branches of Families 1, 3, 5. Similar to Figure 6, except for lower branches instead of upper branches with (a) Family 1, $\lambda_1 = 0.3012$, (b) Family 3, $\lambda_1 = 0.0066$, (c) Family 5, $\lambda_1 = 0.00014$. The only exception is the bottom right panel of (c). For the corresponding ODE initial conditions and dynamics see the bottom panels (left of the vertical line) in each of Figures 6, 7, and 8.

through interaction (and perhaps the dominance of the most unstable mode of the highest growth rate) to move in the opposite direction, diverging away from the center.

We now turn to a description of the lower branches and their dynamics for these families for reasons of completeness. This is shown in Fig. 9. Panel (a) in the figure shows the 2 kink dynamics in family 1. The relevant unstable (saddle) configuration either destabilizes with the kinks moving outward, or does so with them moving inward (toward the center) colliding at $x = 0$ and then subsequently moving outward. Similar examples are shown in panel (b) for the case of family 3. The only difference in this case is that when the kinks move inward, they encounter a higher barrier (that imposed by the solution of family 1) and hence get trapped in the well between family 3 and family 1. This is the well involving the stable solution of the family 2 around which the dynamics ends up orbiting in the bottom right panel (b). Finally, a similar phenomenology is present in the case of panel (c). Interestingly, in this case, the oscillation is between family 5 and family 3 unstable saddle configurations, which means that the dynamics is orbiting around the center (stable) configuration of family 4.

C. Families 2 and 4

Lastly, we briefly refer to families 2 and 4, showcased in Fig. 10. Here, as explained at the level of the theoretical analysis of the energy landscape, but also corroborated by related numerics of the unstable families, the lower branches concern solutions that are stable. Indeed these are center configurations (around which the dynamics may orbit, as a result of the instability of the saddles above). This is reflected in the stable nature of the two bottom right subplots in panels (a) and (b) within Fig. 10. As before, crossing through negative β_2 in both families leads to modulationally unstable backgrounds with continuous spectrum crossing through to the real line. Past the turning point, we revert to the upper branches for each configuration which look fairly similar and essentially differ in the location of the resulting 6 kinks. Interestingly the inner kinks remain at the same distance as for the stable lower branch (for each of the families 2 and 4) and two outer pairs of kinks are added to the configuration at larger distances.

As regards the upper branches of each of these families, panels (c) and (d) of Fig. 10 reflect the theoretical predictions for their stability. In each case there are two unstable modes (rather than 3) which, in fact, have very proximal eigenvalues. It is for that reason that these two pairs of real modes cannot be distinguished in the two upper right insets of panels (a) and (b). Recall that the oscillatory instabilities are not systematically considered here given their size dependence. The other 3 pairs of nonzero modes of the 6-kink system are imaginary and are also given in panels (c) and (d). In either case, the destabilizing eigenmodes are similar and involve either an in-phase motion of the inner 2 kinks while the outer 4 ones are moving in the opposite direction or an out-of-phase motion of the inner kinks which on each “side” (i.e., for $x > 0$ or $x < 0$) is opposite to the motion of the outer kinks. For brevity, we do not present the dynamical implementation of these cases, although a similarly good agreement with the predictions of the theory has been found in this case.

Indeed, we elaborate a bit further on the quantitative aspects of the comparison of the theory with our numerical computations now. This comparison can be seen as summarized in the two extensive tables I and II. The former of

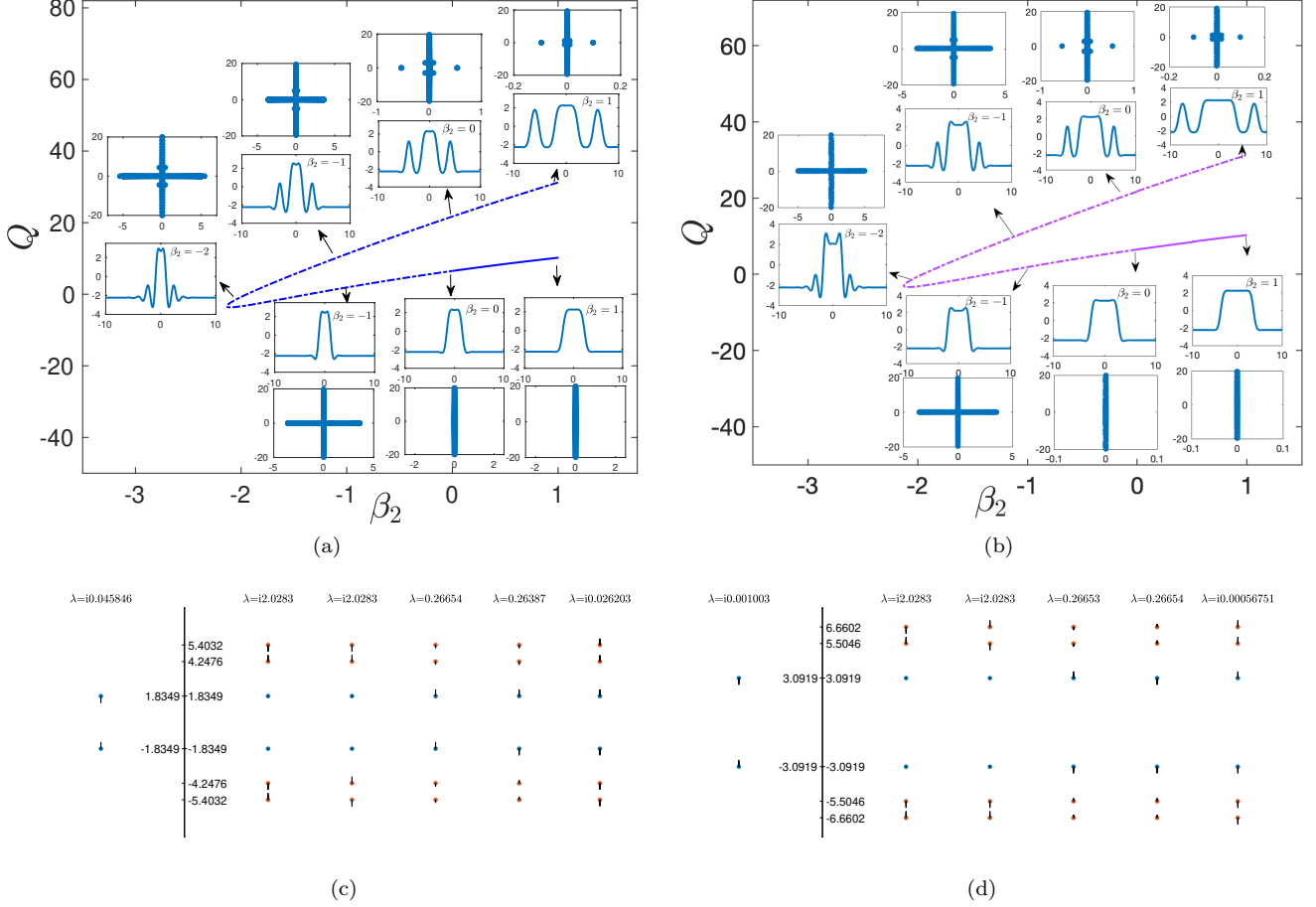


FIG. 10. Bifurcation diagrams and the corresponding steady state solutions and spectra for (a) Family 2 (b) Family 4. The former are presented in the format shown previously of Q vs. β_2 . The latter indicate the eigenvalues and prescribe the motion of the solitary waves, in line with the desired eigenmode.

these tables offers the comparison of the equilibrium configurations in the context of the ODE theoretical approach of section IIB and the full PDE results. In the latter, the zero crossings of configurations with 2 (all lower branches), 4 (upper branches of families 0 and 3) and 6 kinks (remaining upper branches) have been identified and listed. One can observe a very good agreement between the two. This only deteriorates a little in the cases of outermost kinks but is still qualitatively excellent and even quantitatively satisfactory.

An even more stringent test of the theory (in comparison to equilibrium positions of ODE vs. PDE) consisted of the examination of the relevant internal modes of vibration presented in Table II. Here, we have included for completeness the motion induced by the mode (e.g., as we have already discussed, all lower branch non-vanishing modes should be out-of-phase), as well as the spatial parity of the mode. The former motion is useful towards understanding the unstable dynamics induced by the mode (this was also explained in the discussion of the different families above). The latter is in line with the expectations of Sturm-Liouville theory, wherever appropriate (given the 1d nature of our system). Remarkably, we see that in this case as well, the effective particle method of Section IIB is fairly accurate in its prediction of both the oscillatory and the growing modes of the system. As the table shows, this turns out to be the case for both lower and upper branches, and for all the different families considered from 0 to 5. It is important to note here that for the real modes, such a comparison is relatively straightforward as the modes are separated from the rest of the spectrum. However, such a comparison is far more involved when we are, in principle, seeking localized modes involving relative kink motions “buried” within the continuous spectrum. Nevertheless, we have developed a technique based on the inverse participation ratio (IPR) [29] which enables us to identify modes with high IPR, even when embedded in the continuous spectrum, and to compare them favorably in many cases with the theoretical predictions. We now briefly discuss the associated details.

Family	Branch	Soliton Position	
		ODE	PDE
0	lower	0.5778	0.6084
	upper	1.2063	1.2229
		2.3620	2.4389
1	lower	1.2063	1.20534
	upper	1.2063	1.20493
		3.6190	3.63302
		4.7747	4.84924
2	lower	1.8349	1.83539
	upper	1.8349	1.83495
		4.2476	4.26350
		5.4032	5.47906
3	lower	2.4634	2.46336
	upper	0.5778	0.60799
		2.9905	3.03715
4	lower	3.0919	3.09138
	upper	3.0919	3.27728
		5.5046	5.70647
		6.6602	6.92233
5	lower	3.7204	3.72945
	upper	1.2063	1.22286
		2.3620	2.43858
		4.7747	4.86794

TABLE I. Soliton positions, ODE versus PDE, for $\beta_2 = 0.5$

The Inverse Participation Ratio can be defined for a function $u(x)$ as

$$\text{IPR} = \frac{\int |u|^4 dx}{(\int |u|^2 dx)^2}. \quad (33)$$

When u is an eigenvector (eigenfunction), this quantity can be used to find eigenvectors that are the most localized, even when there is a continuous background present. We create an IPR plot, which gives the IPR value for each eigenvector, listed in order of the corresponding eigenvalue (using Matlab’s default method of ordering complex eigenvalues). An example, corresponding to Family 1, upper branch, is given in Figure 11. Since the eigenvalues come in pairs (\pm pairs for the real eigenvalues and complex conjugate pairs—in fact, quartets $\pm\lambda_r \pm i\lambda_i$ —for the complex valued ones), only the first of each pair that “stands out” from the others is marked with an asterisk and labeled with its eigenvalue. From this plot we infer that three real and one purely imaginary eigenvalue correspond to the most localized eigenvectors. Note that the slightly elevated parts of the graph near eigenvalue order number 1130 correspond to eigenvalues that have both non-zero real and imaginary parts (which are not considered) and the elevated part near 1200 corresponds to a zero eigenvalue (representing translational invariance). Thus, the four eigenvalues identified in the figure are the ones listed in Table II. Also note that the eigenvalue $2.2871 i$ listed in Table II has an asterisk, indicating that it does not correspond to an elevated IPR value.

Figure 12 shows the dynamics for several embedded (purely imaginary) eigenvalues. The plots in the first (left) column verify that for typical lower branch cases, pure oscillations occur for long periods of time, with the frequency given by the corresponding eigenvalue (the top left plot is also, in fact, unchanged up to $t = 300$). The plots in the second column show that for typical upper branch plots, the expected oscillations (with frequencies corresponding to the—imaginary part of the— respective eigenvalues) occur for short periods of time, after which nonlinearity takes over as the solitary wave paths start to interact. The blue curves track the centers of the kinks, and are needed as the contour plots do not have fine enough resolution to show the oscillations. The oscillations manifested in these graphs (and their localized nature around the kink equilibria) confirm that the modes selected by the high IPR are embedded ones within the continuous spectrum associated with the effective normal modes of the kink-antikink interacting particle system.

Family	Branch	Eigenvalues		Soliton Initial	PDE Eigenvector
		ODE	PDE	Directions	Symmetry
0	lower	2.0337 i	2.0263 i	↓↑	even
	upper	0.2139	0.2231	↓↓↑↑	even
		2.0337 i	2.2072 i *	↑↓↓↑	odd
		2.0227 i	2.2481 i *	↓↑↓↑	even
1	lower	0.30996	0.30119	↓↑	even
	upper	0.39091	0.38075	↓↓↑↓↑↑	even
		0.26654	0.26383	↑↑↓↓↑↑	odd
		0.11958	0.12634	↓↓↑↑↑↑	even
		2.0284 i	2.0334 i	↑↓↓↓↑↑	odd
		2.0284 i	2.2871 i *	↓↑↑↓↑↑	even
2	lower	0.04585 i	0.04460 i	↓↑	even
	upper	0.26654	0.26401	↑↑↓↓↑↑	odd
		0.26387	0.26168	↓↓↑↓↑↑	even
		0.02620 i	0.02721 i	↓↓↑↑↑↑	even
		2.0283 i	2.0418 i	↓↑↑↓↑↑	even
		2.0283 i	2.2842 i *	↑↓↓↓↑↑	odd
3	lower	0.006781	0.00660	↓↑	even
	upper	0.30542	0.30825	↑↓↓↑	odd
		0.22037	0.21038	↓↑↓↑	even
		2.0227 i	2.2318 i *	↓↓↑↑	even
4	lower	0.001003 i	0.000976 i	↓↑	even
	upper	0.26653	0.26407	↓↓↑↓↑↑	even
		0.26654	0.26402	↑↑↓↓↑↑	odd
		0.00057 i	0.00021	↓↓↑↑↑↑	even
		2.0283 i	2.0367 i	↓↑↑↓↑↑	odd
		2.0283 i	2.2784 i *	↑↓↓↓↑↑	even
5	lower	0.00014	0.00014	↓↑	even
	upper	0.30393	0.31054	↓↑↑↓↑↑	even
		0.26654	0.26397	↑↓↓↓↑↑	odd
		0.15465	0.15087	↓↓↑↑↑↑	even
		2.0283 i	2.2992 i *	↑↑↓↓↑↑	odd
		2.0171 i	2.0213 i	↓↑↑↓↑↑	even

TABLE II. ODE versus PDE eigenvalues and PDE eigenvector symmetry for $\beta_2 = 0.5$. The PDE eigenvalues listed are those that were identified using an inverse participation ratio (IPR) plot; * represents eigenvalues that were not apparent from the IPR plot, but were the closest PDE eigenvalues to the corresponding ODE eigenvalues that also had the same initial direction signature.

Lastly, we should mention that in addition to exploring the growth rate of unstable configurations via spectral stability analysis, we have also resorted to an alternative method to corroborate our numerical stability results through direct numerical simulations. Indeed, we have considered a method of perturbing the unstable eigenvectors and subsequently monitoring the instability growth rates. Typical case examples of the corresponding results are shown in Fig. 13. Here, we compare the findings of the linear stability computations (via red solid lines) with the PDE simulations (via blue lines). In each case the blue lines represent the projections arising from subtracting from $u(x, t)$ the equilibrium solution u_0 and then projecting the difference to the instability eigenvector. With the dotted blue lines, we represent the dynamical outcome of positive perturbations, while with the dash-dot blue lines the case of a negative perturbation. The the red lines represent a least-squares straight line fit to the linear part of the blue curves in these semilog plots. In this way, we can corroborate the growth rate observed in the spectral analysis via the instability dynamics observed in the full PDE model. In essentially all the cases considered the agreement is found to be very good with respect to our theoretical expectations.

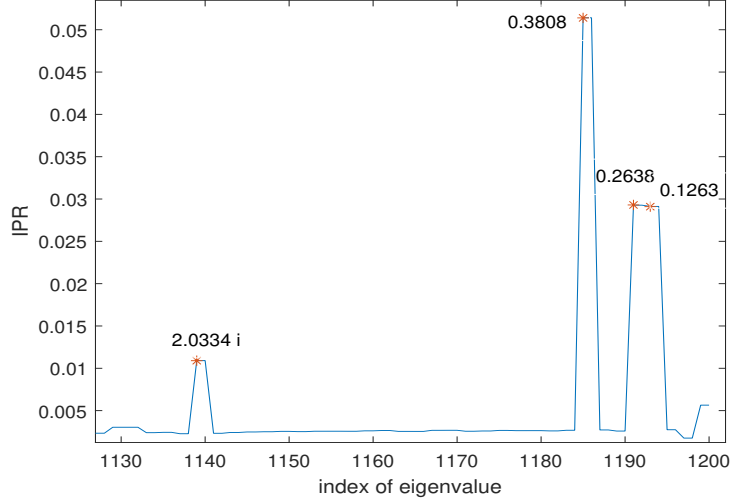


FIG. 11. Inverse Participation Ratio plot for Family 1, upper branch. Numerical values shown are eigenvalues corresponding to the eigenvector whose IPR is calculated and plotted. Eigenvectors with index values smaller than shown do not contribute significant IPR values.

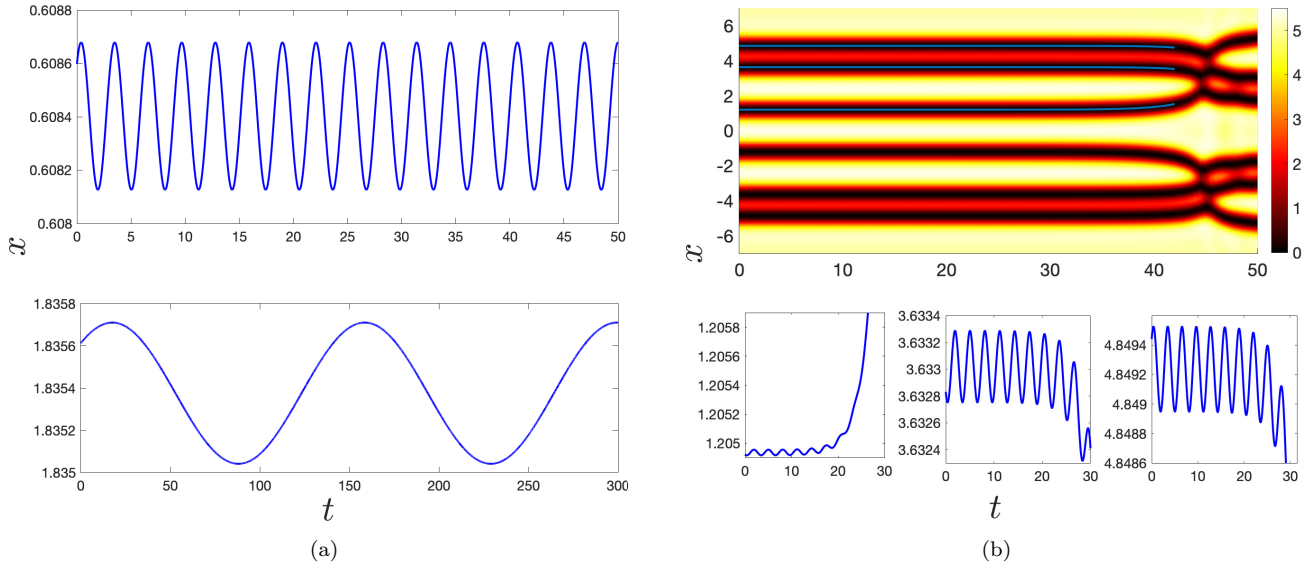


FIG. 12. Dynamics corresponding to imaginary eigenvalues that are embedded in the continuous spectrum. In each case a small amount of an eigenvector with imaginary eigenvalue is added to the steady state, inducing an out-of-phase oscillation for a pair of solitons. The two panels in (a) represent out-of-phase oscillations for Families 0 (top figure, eigenvalue 2.0263) and 2 (bottom figure, eigenvalue 0.0446), both for the bottom branch. We show only the curve that represents the center of the soliton that appears on the positive side of the x -axis (and hence on top in the contour plots). All figures in (b) represent Family 1, top branch, with eigenvalue 2.0334. The three blue curves on the bottom again represent the motion of the center of each of the three solitons that appear on the positive side of the x -axis (corresponding to the top three solitons in the contour plot shown). These blue curves also appear superimposed on the contour plot, where due to scaling, the oscillations are not apparent.

IV. CONCLUSIONS AND FUTURE CHALLENGES

In the present work we have revisited the topic of media with competing quadratic and quartic dispersions in the context of nonlinear structures commonly considered in self-defocusing media, namely kink-like states in the form of

dark solitary waves. We have focused our attention, in particular, on the setting of multiple such structures and have proposed a systematic understanding of pairs of such kinks on the basis of an energetic landscape emanating from the kink-antikink interaction. The competition of the different dispersions, and indeed crucially the presence of the quartic effects enable the presence of oscillatory tails and of potential bound states for multi-kink states. We have analyzed the first few center- and saddle-configurations of this type, indeed 3 center states (families 0, 2, 4) and 3 saddle ones (families 1, 3, and 5). In addition to presenting a systematic continuation of the states in one of the most natural parametric variations of the system (the coefficient of the quadratic dispersion), we have followed the solutions past their (typical, aside from family 0) turning points, identifying their respective upper branches, unveiling, in turn, solutions associated with 4, as well as with 6 kinks.

We have provided a systematic particle picture that offers the possibility of a systematic classification of the obtained states, irrespective of the number of kinks based on their interactions, provided that the kinks are sufficiently well separated, i.e., for large enough positive quadratic dispersion β_2 in our system. This analysis was used to accurately capture the equilibrium distance of the kinks, as well as their internal excitation modes. In a wide range of corresponding families and examples, stable and unstable, lower and upper branch ones, the method was found to provide systematic insights regarding the kink dynamics and their stability.

Our considerations offer a systematic view of the possible stationary multi-soliton solution families and can be naturally extended to either higher-order families or heteroclinic ones involving an odd number of kinks. Both directions have been successfully attempted, although they are not detailed herein. It should be added here that while in the present manuscript we have taken an approach that is more mathematically formal and is driven by our numerical computations, the relevant considerations are well-positioned to be explored on the basis of rigorous mathematical theory in the context of the so-called Lin's method allowing for the consideration of existence of multi-solitary wave solution [30, 31]. Such an approach has recently been extended to kinks in conservative systems in connection to their existence and stability (in fact, in a discrete realm) by some of the present authors [32]. It would be a very relevant comparison for the present work if such a method was applied to the context of the model considered herein. Yet another consideration suggested by our results involves the setting of traveling excitations. In addition to the loss of Galilean invariance (in the presence of quartic dispersion) [19] rendering interesting the existence and stability analysis of single traveling kinks, we have found that bound, breathing states of two kinks are quite common and would be worth seeking as potentially exact solutions and to understand their stability. Such waveforms would be time-periodic in a co-traveling frame, a feature that would necessitate their consideration under the prism of Floquet theory. In an additional dimension of considerations —pun intended—, the study of coherent structures in higher-dimensional, such as vortices in media with competing dispersion operators would naturally also be a direction of particular interest. Some of the above studies are currently in progress and will be presented in future publications.

Acknowledgements. This material is also based upon work supported by the US National Science Foundation under Grant Nos. DMS-2204702 and PHY- 2110030 (P.G.K.).

-
- [1] C. Sulem and P.L. Sulem, *The Nonlinear Schrödinger Equation*, Springer-Verlag (New York, 1999).
 - [2] M.J. Ablowitz, B. Prinari and A.D. Trubatch, *Discrete and Continuous Nonlinear Schrödinger Systems*, Cambridge University Press (Cambridge, 2004).
 - [3] M. J. Ablowitz, *Nonlinear Dispersive Waves: Asymptotic Analysis and Solitons*, Cambridge University Press (Cambridge, 2011).
 - [4] C.J. Pethick and H. Smith, *Bose-Einstein condensation in dilute gases*, Cambridge University Press (Cambridge, 2002).
 - [5] L.P. Pitaevskii and S. Stringari, *Bose-Einstein Condensation*, Oxford University Press (Oxford, 2003).
 - [6] P. G. Kevrekidis, D. J. Frantzeskakis, and R. Carretero-González, *The defocusing nonlinear Schrödinger equation: from dark solitons and vortices to vortex rings*, SIAM (Philadelphia, 2015).
 - [7] A. Hasegawa, *Solitons in Optical Communications*, Clarendon Press (Oxford, NY 1995).
 - [8] Yu.S. Kivshar and G.P. Agrawal, *Optical solitons: from fibers to photonic crystals*, Academic Press (San Diego, 2003).
 - [9] M. Kono and M. M. Skorić, *Nonlinear Physics of Plasmas*, Springer-Verlag (Heidelberg, 2010).
 - [10] A. Blanco-Redondo, C. Martijn de Sterke, J.E. Sipe, T.F. Krauss, B.J. Eggleton, and C. Husko, *Nature Communications*, **7**, 10427 (2016).
 - [11] A.F.J. Runge, D.D. Hudson, K.K.K. Tam, C.M. de Sterke, A. Blanco-Redondo, *Nature Photonics* **14**, 492 (2020).
 - [12] A.F.J. Runge, Y.L. Qiang, T.J. Alexander, M.Z. Rafat, D.D. Hudson, A. Blanco-Redondo, and C.M. de Sterke, *Phys. Rev. Research* **3**, 013166 (2021).
 - [13] K.K.K. Tam, T.J. Alexander, A. Blanco-Redondo, and C.M. de Sterke, *Phys. Rev. A* **101**, 043822 (2020).
 - [14] R.I. Bandara, A. Giraldo, N.G.R. Broderick, and B. Krauskopf, *Phys. Rev. A* **103**, 063514 (2021).
 - [15] R. Parker and A. Aceves, *Phys. D* **422**, 132890 (2021).
 - [16] T.J. Alexander, G. A. Tsolias, A. Demirkaya, Robert J. Decker, C. Martijn de Sterke, and P. G. Kevrekidis, *Opt. Lett.* **47**, 1174-1177 (2022).
 - [17] G.A. Tsolias, R.J. Decker, A. Demirkaya, T.J. Alexander, and P.G. Kevrekidis, *J. Phys. A: Math. Theor.* **54**, 225701 (2021).
 - [18] A.F.J. Runge, T.J. Alexander, J. Newton, P.A. Alavandi, D.D. Hudson, A. Blanco-Redondo, and C.M. de Sterke, *Opt. Lett.* **45**, 3365-3368 (2020).
 - [19] J. Widjaja, E. Kobakhidze, T.R. Cartwright, J.P. Lourdesamy, A.F. J. Runge, T.J. Alexander, and C.M. de Sterke *Phys. Rev. A* **104**, 043526 (2021)
 - [20] V. Karpman, *Phys. Lett. A* **193**, 355 (1994).
 - [21] V.I. Karpman, *Phys. Rev. E* **53**, R1336 (1996).
 - [22] A. Demirkaya and M. Stanislavova, *DCDS-B* **24**, 197 (2019).
 - [23] I. Posukhovskiy and A. Stefanov, *DCDS-A* **40**, 4131 (2020).
 - [24] A. Stefanov, G.A. Tsolias, J. Cuevas-Maraver, P.G. Kevrekidis *J. Phys. A: Math. Theor.* **55** 265701 (2022).
 - [25] D. J. Frantzeskakis, *J. Phys. A-Math. Theor.* **43**, 213001 (2010).
 - [26] N. S. Manton, *Nuclear Phys. B* **150**, 397 (1979).
 - [27] I.V. Barashenkov, *Phys. Rev. Lett.* **77**, 1193 (1996)
 - [28] M. Johansson, Yu.S. Kivshar, *Phys. Rev. Lett.* **82**, 85 (1999).
 - [29] B. Kramer and A. MacKinnon, *Rep. Prog. Phys.* **56**, 1469 (1993).
 - [30] X. B. Lin, *Proc. Roy. Soc. Edinburgh A* **116**, 295 (1990).
 - [31] B. Sandstede, *Trans. Amer. math. Soc.* **350**, 429 (1998).
 - [32] R. Parker, P.G. Kevrekidis, A. Aceves, *Nonlinearity* **35**, 1036 (2022).

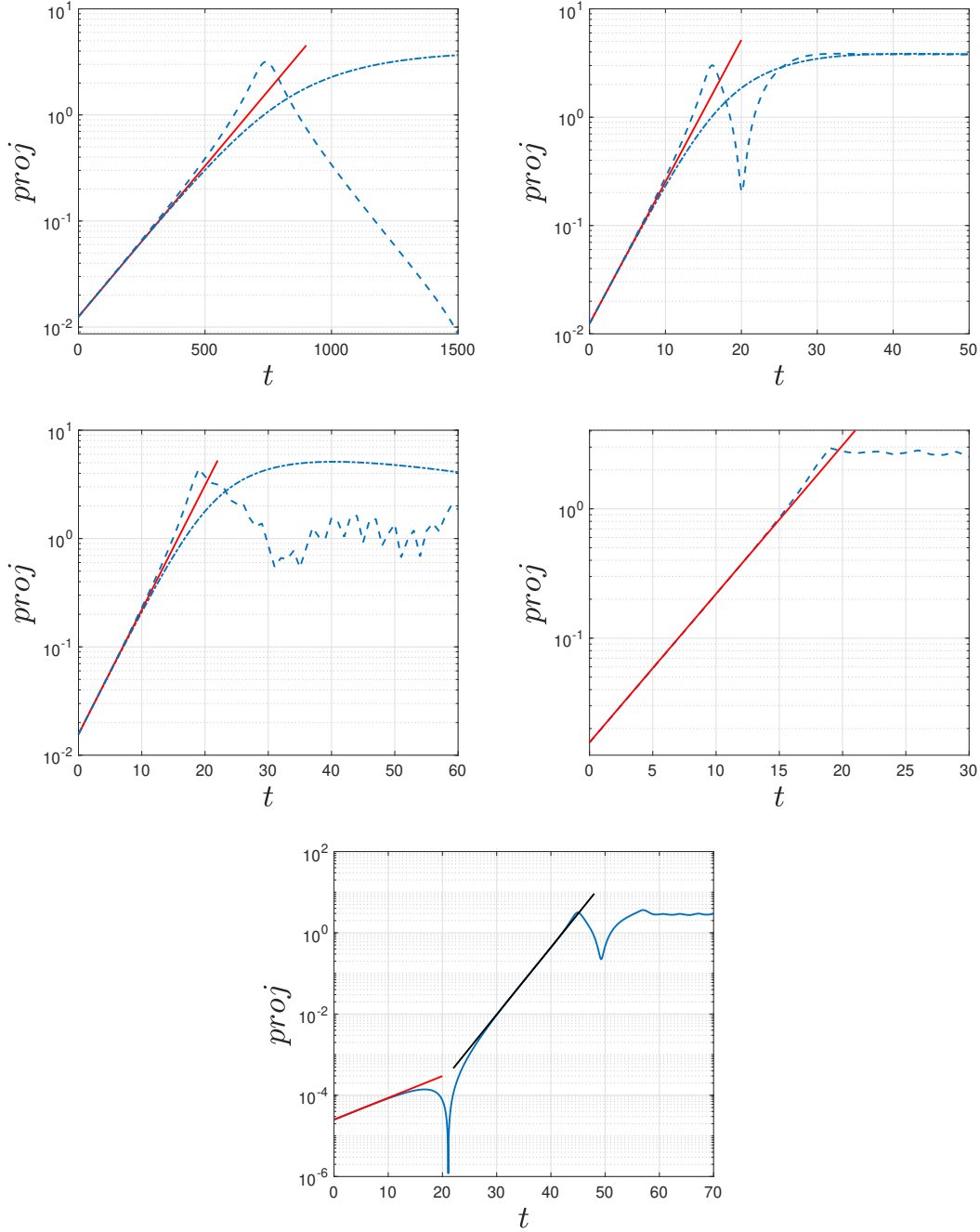


FIG. 13. Projection plots for $\beta_2 = 0.5$. In the top two rows, for a few selected solutions $u(x, t)$, we plot the scalar projection of $u(x, t) - u_0(x)$ in the direction of an eigenvector (as a function of time) using a semilog scale. For these solutions, the initial steady state $u_0(x)$ was slightly perturbed in the direction of said eigenvector. In each case the blue lines represent the projections, with the dotted blue lines representing positive perturbations, the dash-dot blue lines representing a negative perturbation; the red lines represent a least-squares straight line fit to the linear part of the blue curves. We observe a linear portion near the beginning of each plot, whose slope matches very closely with what is predicted by the corresponding eigenvalue. In all cases the slope of the projection curve matches the eigenvalue to two (for the smallest eigenvalues) or three decimal places. The cases are as follows. First row - steady state 3 (left) and steady state 1 (right), both lower branch (note the different time scales). Second row - steady state 4, largest real eigenvalue (left - even eigenvector) and steady state 4, second largest real eigenvalue (right - odd eigenvector - projections coincide). The figure in the third row shows how an initial (small) growth rate can transition to a larger growth rate (projection in blue). This figure corresponds to family 1, upper branch where the initial growth rate of 0.124 (fitted line in red) transitions to a growth rate of 0.381 (fitted line in black). Here $u_0(x)$ was perturbed in the direction of the eigenvector with eigenvalue 0.12634 and then projected onto the eigenvector with eigenvalue 0.38075.